9-2020

Evaluation Of Mechanical and Biocompatibility Properties of Hydroxyapatite/Manganese Dioxide Nanocomposite Scaffolds for Bone Tissue Engineering Application

Fatemeh Azizi

Fatemeh Heidari

Farahnaz Fahimipour

Mohammad Sajjadnejad

Daryoosh Vashaee

See next page for additional authors

Authors

Fatemeh Azizi, Fatemeh Heidari, Farahnaz Fahimipour, Mohammad Sajjadnejad, Daryoosh Vashaee, and Lobat Tayebi

Evaluation Of Mechanical and Biocompatibility Properties of Hydroxyapatite/Manganese Dioxide Nanocomposite Scaffolds for Bone Tissue Engineering Application

Fatemeh Azizi
Department of Materials Engineering, School of Engineering, Yasouj University, Yasuj, Iran
Fatemeh Heidari
Department of Materials Engineering, School of Engineering, Yasouj University, Yasuj, Iran
Farahnaz Fahimipour
Marquette University School of Dentistry, Milwaukee WI
Dental Biomaterials Department, School of Dentistry, Tehran University of Medical Sciences, Tehran, Iran
Mohammad Sajjadnejad

Department of Materials Engineering, School of Engineering, Yasouj University, Yasuj, Iran

Daryoosh Vashaee

Department of Electrical and Computer Engineering, NC State University, Raleigh NC

Lobat Tayebi

Marquette University School of Dentistry, Milwaukee WI

Abstract

The aim of this research was to evaluate the mechanical properties, biocompatibility, and degradation behavior of scaffolds made of pure hydroxyapatite (HA) and HA-modified by MnO_2 for bone tissue engineering applications. HA and MnO_2 were developed using sol-gel and precipitation methods, respectively. The scaffolds properties were characterized using X-ray diffraction (XRD), Fourier transform spectroscopy (FTIR), scanning electron microcopy (SEM), energy dispersive spectroscopy (EDS), and transmission electron microscopy (TEM). The interaction of scaffold with cells was assessed using in vitro cell proliferation and alkaline phosphatase (ALP) assays. The obtained results indicate that the HA/ MnO_2 scaffolds possess higher compressive strength, toughness, hardness, and density when compared to the pure HA scaffolds. After immersing the scaffold in the SBF solution, more deposited apatite appeared on the HA/MnO_2, which results in the rougher surface on this scaffold compared to the pure HA scaffold. Finally, the in vitro biological analysis using human osteoblast cells reveals that scaffolds are biocompatible with adequate ALP activity. [ABSTRACT FROM AUTHOR]

Keywords: biocompatibility; cold isostatic pressing; mechanical properties; nanocomposite

INTRODUCTION

The bone is the main organ of the skeletal body, which supports soft tissues and includes the bone marrow that is the site of the formation of blood cells.[1] When a bone breaks, bone fields are destroyed and the damaged area around the bone cells die. In many fractures and bone injuries, there is a need for alternative or filler materials to repair bone tissue.[2,3] So far, various engineering materials, including ceramic materials, metals (alloys), polymers, and composites, have been selected as bone tissue repairers. The bulk of the bone tissue is composed of hydroxyapatite (HA) bioceramic with the chemical formula $Ca_{10}(PO_4)_6(OH)_2$, which is a mineral component of bone with low crystallinity HA and has strengthened its collagen fibers.[4,5] Two-phase calcium phosphate ceramics are a mixture of two phases of HA and beta-tri calcium phosphate, which are commonly used in bone repair. By changing the ratio of HA to beta-tricalcium phosphate, it is possible to control the bioactivity of these types of ceramics. Changing this ratio changes the chemical properties of this substance.[6] HA is used for bone tissue engineering due to its excellent biocompatibility and bone mineralization, bioactivity, non-toxicity and non-inflammation and immunology in bone tissue engineering.[7-9] Although the elasticity modulus of HA is higher than the bone, it alone does not have the mechanical properties of the bone. HA has an inherently fragile structure, which limits its application to areas of the body that are under high loads. Many studies have been done to improve the mechanical properties of HA. One way to overcome this limitation is to use HA as a matrix in a composite and to use biocompatible or bioactive reinforced materials. Therefore, the reinforcement materials in HA matrix are chosen in such a way that their final modulus of elasticity is as close as possible to the bone elastic modulus.[10,11]

Manganese dioxide (MnO_2) has excellent performance in terms of availability, economic efficiency, nontoxicity,[12,13] biocompatibility[14,15] and is environmentally friendly.[16] The structure of MnO_2 is micro-porous.[17] Correction of the particle surface of the HA with MnO_2 reduces the temperature of the sintering, thereby increasing the density of HA. Bones and teeth have about a total of 20 mg of Manganese. Manganese in the bone reduces bone resorption and also plays an important role in immune response, homeostasis of glucose, ATP regulation, reproduction, digestion, and bone growth, and has a significant effect on bone growth. Therefore, the placement of manganese compounds along with the structure of apatite is of great importance, since the behavior and properties of HA are more similar to bone. Manganese also activates the function of the formation of cartilage in bone and skin and synthesis of various enzymes for bone formation.[18-20] Manganese also has antioxidant activities.[22] Studies have shown that HA doped with Mn promotes osteoblast proliferation and activates their metabolism and differentiation.[22] In this study, HA was synthesized by sol-gel method. In fact, sol-gel is the most commonly used method for the production of nanoparticles in the liquid phase due to the lack of special equipment and the ease of process steps, the acceleration of bone treatment and the reduction of bio-contamination.[22]

The cold isostatic pressing (CIP) method is applied in such a way that the pressure is applied simultaneously and uniformly from all directions while all the friction of the sample with the mold wall is completely eliminated. To compress simple or even relatively complex shapes by this method, the dry powders are poured into a flexible metal mold and filled. Then, by pressing the die piston, the sample is formed into a disk or cylinder, enclosed in latex, and thrown into the CIP oil tank. Inside the tank, the latex content of the sample is completely surrounded by hydraulic fluid. After applying pressure, the sample is removed from the machine. This sample does not have enough cohesion and must be sintered. Typically, the pressures in CIP can be ~70 MPa, although pressures > 100 MPa to ~400 MPa are often used. The most important characteristics of pressed ceramic bodies produced by CIP method include dimensional accuracy, robustness and high density. High production speed and cost savings have made it widely used in the ceramic industry.[23,24] For this reason, CIP method was used to prepare the scaffold in this study.

This study intends to modify the HA nanoparticles with MnO_2 nanoparticle precipitation. To construct the scaffolds, the CIP was used, and then the samples were sintered at 1300°C. Microstructure, biodegradability, biocompatibility, and mechanical properties of scaffolds were then investigated.

## MATERIALS AND METHODS

Material preparation

HA synthesis

Nano-HA was prepared by sol-gel method, as described previously.[25] Briefly, $Ca(NO_3)_2.4H_2O$ (0.1 M, Sigma-Aldrich) and $(NH_4)_2HPO_4$ (0.06 M, Sigma-Aldrich) were dissolved in deionized water separately, and the pH of both solutions was adjusted to 11.0 by adding ammonia solution. The solution of $Ca(NO_3)_2.4H_2O$ was dropwise added into the $(NH_4)_2HPO_4$ solution for 1 hour, and the white suspension and gelatinous precipitate were obtained. After aging for 24 hours at room temperature, the precipitates were filtered, washed several times with distilled water and absolute ethanol, dried at 80°C overnight, then calcined at 800°C for 1 hour.

Preparation of MnO 2 -modified-HA powder

250 cc KMnO$_4$ (0.02 M, Sigma-Aldrich) solution was prepared and nano-HA (2 g) was then added into the solution, followed by constant stirring for 2 hours at room temperature. Then, solution was sonicated for 20 minutes and after that stirred for 72 hours again. Finally, the brown precipitates were washed with deionized water and ethanol and dried at 80°C overnight. The obtained powder was calcined at 400°C for 5 hours.[26]

Preparation of MnO 2 modified-HA scaffolds

The prepared MnO$_2$ modified-HA powder was CIP at 250 MPa for 35 seconds. Samples of various tests were made in two forms of disk and cylinder with CIP device. The pressed powder was then sintered at 1300°C for 2.5 hours in a box furnace at a heating rate of 5°C/min. Next, the samples in the shape of circular discs were produced for hardness or compression tests. Figure 1 shows prepared samples for hardness and compressive tests.
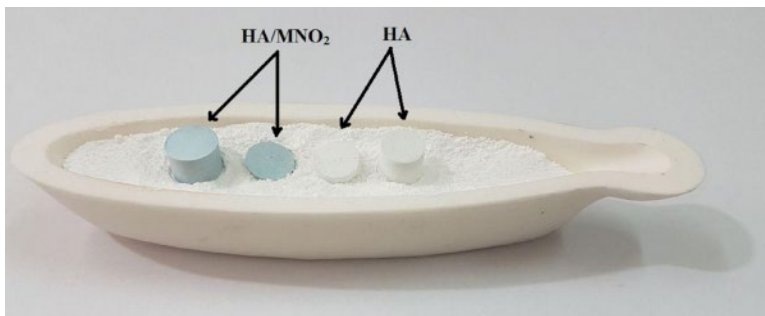
1 Prepared samples for compressive and hardness tests

Material characterization

To investigate the phase composition of extracted HA powder, XRD: (Bruker-AXS-D8-Discover) analysis was carried out before and after sintering the HA. The XRD system works with voltage and current setting of 40 kV and 40 mA, respectively, with parallel graphite monochromator and uses CuKα radiation (1.5406 Å). For qualitative analysis, XRD diagrams were recorded in the interval 20-65°, with a step size of 0.02°.

To identify the existence of organic species, along with the degree of probable dehydroxylation of HA during the heat treatment, Fourier transform infrared (FTIR: Shimadzu 8300) analysis was performed. The measurements were carried out in the transmission mode in the mid-infrared range with wave numbers from 400 to 4000 cm^{-1}. To record the FTIR spectrum of each sample, 3 mg of the powder was mixed and pressed with 300 mg of KBr to obtain a pellet for FTIR analysis.

A scanning electron microscope (SEM) equipped with energy dispersive spectroscopy (EDS) was used to examine the morphology of the powder and scaffolds. The porosity of scaffolds was also investigated by SEM.

A transmission electron microscope (JEOL JEM-2100 TEM) was used to assess the nanoparticles' morphology and size in the MnO$_2$ modified HA scaffolds.

The XRD chart was plotted by Xpert software. Spectra from FT-IR analysis were plotted by Spectra Analysis software. Stress-strain diagrams derived from pressure test, thermal gravimetric analysis-

differential scanning calorimetry (TGA-DSC) diagram and cell culture diagrams were plotted by origin.2018 software.

Mechanical properties

Mechanical properties of the samples were evaluated with compressive and hardness tests. The compressive test was performed on cylindrical samples (10 mm in diameter × 10 mm in length) using a universal testing machine (Zwick, Material Prufung, 1446e60) with a 10 kN load cell. Although the best sample for compression test is a diameter-to-height ratio of 1/2, in the ceramic samples, we can also test the compression with a diameter-to-height ratio of 1.27 The crosshead speed was 0.5 mm/min. The surface area under the stress-strain curves was calculated and considered as the toughness of the samples. Disc shape samples were selected for microhardness test (16 mm diameter × 4 mm height). The microhardness (Hv) of the polished sintered samples was determined via the Vickers indentation (MHV1000Z) using an applied load of 200 g with a dwell time of 10 seconds. The density of samples was measured by Archimedes method.

In vitro biodegradability

The sintered HA samples were soaked in 20 mL of simulated body fluid (SBF) with pH 7.40 and specific ion concentrations nearly identical to those in human blood plasma (Na^+ 140.3 mm, K^+ 5.3 mm, Mg^{2+} 1.3 mm, Ca^{2+} 2.2 mm, Cl^- 148.0 mm, HCO_3^- 4.0 mm, HPO_4^{2-} 0.8 mm, SO_4^{2-} 0.5 mm). After the samples were kept at 37°C for 28 days, they were removed from SBF, gently rinsed with distilled water and dried at room temperature. The changes in the surface morphologies of samples before and after soaking in the SBF were characterized by SEM and EDX.

Cell culture

To sterilize the samples, they were immersed in 70% ethanol three times, followed by washing with phosphate buffer saline (PBS) for 15 min/cycle. The culture medium was prepared from Dulbecco's Modified Eagle's Medium (DMEM, Sigma) supplemented with 10% fetal bovine serum (FBS, Sigma) and 1% Penicillin-Streptomycin (Invitrogen). 5×10^5 Human Osteoblast Cells (HOB, Cell Applications) were cultured on the samples immersed in growth medium. The medium was refreshed every 2 days.

The morphology of HOB cells cultured on the samples was studied by scanning electron microscopy (SEM, JEOL JSM-6510LV) after 14 days' culture. To prepare the samples for SEM imaging, they were removed from the culture medium, rinsed in PBS and cells were fixed with 10% formaldehyde solution. The samples were then dehydrated in gradient ethanol concentrations of 50, 70, 80, 90, and 100% to protect their intact morphology. The samples were coated with gold using a GSL-1100X-SPC12 Compact Plasma Sputtering Coater instrument, prior to SEM imaging. ProstoBlue® (PB) cell vitality (Invitrogen) was performed according to the manufacturer's protocols at time intervals of 7 and 14 days after cell seeding. The samples were sterilized using 70% ethanol. The samples were then placed in a non-adherent 24 well-plate and 5×10^5 HOB cells were seeded on the samples. The culture medium was changed every 2 days.

The fluorescence intensity (Ex: 560 nm and Em: 590 nm) was measured by a spectrophotometric plate reader (Synergy HTX, BioTEK). Triplicate samples were used for this experiment.

Alkaline phosphatase activity

Alkaline phosphatase activity (ALP) of HOB seeded samples was performed using an ALP assay kit (Abcam) after 14 days. The seeded cells on the samples were lysed with RIPA lysis and extraction buffer (Invitrogen). Fifty microliter of lysate was reacted with 150 µL of p-nitrophenyl phosphate (p-NPP) for 45 minutes at 37°C. The reaction was terminated with stop solution, and the absorbance intensity of p-nitrophenol was determined at 405 nm, using a microplate reader (Synergy HTX, BioTEK). Cell lysates were investigated for protein content using a micro-BCA assay kit (Pierce), and ALP was normalized to the total protein content, which was measured using Pierce BCA protein assay kit. ALP was expressed in arbitrary units. Triplicate samples were used for this experiment. All data was shown as mean ± standard deviation (mean ± SD). The significant difference was analyzed by one-way ANOVA complemented by Tukey's multiple comparisons test. $P < .05$ were considered as statistically significant.

RESULTS AND DISCUSSION

XRD analysis

Figure 2A,B show the XRD analysis for pure HA and HA/MnO_2. The XRD pattern of these samples shows the following broad diffraction peaks at 26.172, 28.25, 29.1, 31.9, 32.35, 33, 34.2, 39.96, 46.85, 48.25, 50.65, 51.4, 52.35, 63.1, and 53.38° (Figure 2A). All reflections are characteristics of the hexagonal phase of HA $[Ca_{10}(PO_4)_6(OH)_2]$, according to the standard data (JCPDS No. 01-074-0566).[28] The obtained patterns are in agreement with Kim et al[29] and Heidari et al.[30,31] MnO_2 peaks were also seen at angles of 18.20, 28.88, 35.46, 37.5, 41.97, 49.39, and 60.3°.[26,32] Given that the intensity of the peaks of the pattern of Figure 2B is greater than that of Figure 2A, it is concluded that the HA crystallinity increased by adding MnO_2. Additionally, the additional phase of tricalcium phosphate (TCP) in the HA powder was detected at the angles indicated in the pattern of Figure 2A,B (rhombuses on the graph). These peaks, which represent β-TCP, decreased with the addition of MnO_2. The study of the effect of calcination on HA powder showed that β-TCP peak at 800°C began to emerge. The decrease of the β-TCP peak with the precipitation of MnO_2 may be due to the replacement of the Mn ions with Ca ions in the β-TCP phase. The twin Mn ions seem to partially occupy Ca^{2+} sites in the β-TCP structure. Therefore, due to the larger atomic radius Mn than Ca, the intensity of the β-TCP peak is reduced by this replacement.[19] The absence of any peak at 37.5°, indicating CaO, can be due to stoichiometry with a ratio of 1.67 and its conversion to HA. By adding MnO_2 to HA, a distinct color change was observed from white to cream. However, after sintering in the air at 1300°C, the pure HA remained white, while the HA containing MnO_2 changed from cream to blue (Figure 1).
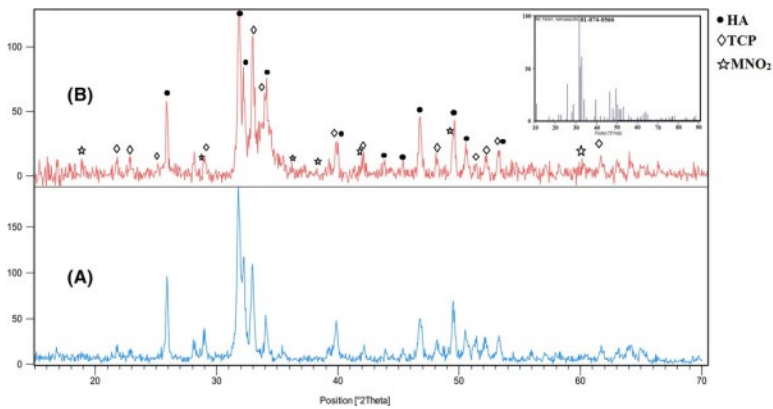
2 XRD pattern of (A) pure HA, (B) HA/MnO₂ composite

FTIR analysis

The stretching band at 3426.89 cm^{-1} and liberation band at 632.537 cm^{-1} originate from OH$^-$ groups. The bands located at 472.474, 568.798, 601.682, 1039.44 and 1091.51 cm^{-1} originate from PO4^{3-} ions, and are weaker than the strong P-O stretching vibration due to HA stoichiometry. The bands at 1400.07 and 1614.13 cm^{-1} originate from CO$_3^{2-}$ ions (Figure 3A). Carbonate ions are a common impurity in both synthetic and natural HA.[27] The FTIR spectrum of the sample that was heat treated at 800°C is in good agreement with the spectrum reported by Heidari et al[27] for natural HA material (see Figure 3A). The peak observed at 580-560 cm^{-1} is related to the vibrational state of Mn-O and confirms the oxidation of Mn[19,33-36] (Figure 3B).
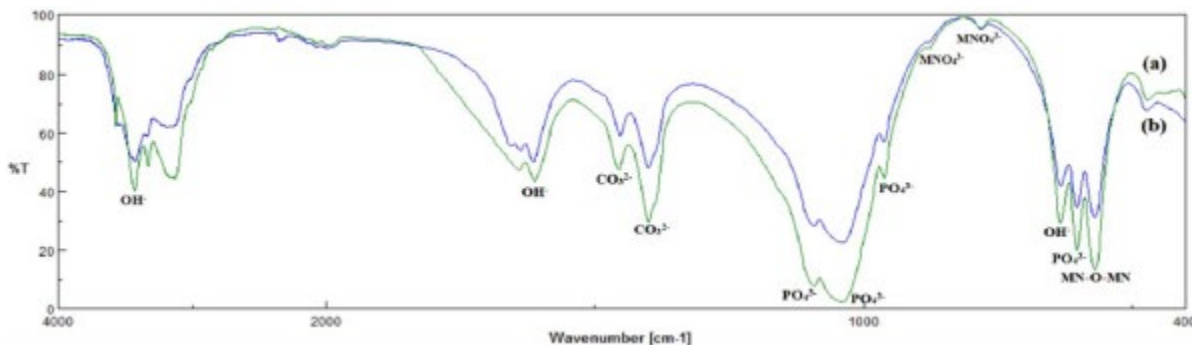

3 FTIR analysis of (A) HA, (B) HA/MnO₂ powder

Scanning electron microscope images

Figure 4A,B show the SEM images of the cross-sectional area of the pure HA and HA/MnO₂ composite samples sintered at a temperature of 1300°C. Results show that modification of HA with MnO₂ reduces the porosity of HA (Figure 4A) and enhances its sinterability (Figure 4B). Royer et al[37] and Wang et al[38] reported that HA degradation began at about 1300°C. In general, sintering HA can result in partial thermal decomposition of HA to TCP or tetra-tricalcium phosphate(TTCP). Thermal decomposition consists of two steps: dehydroxylation and decomposition. Dehydroxylation to oxi-HA at a temperature of about 850-900°C with a completely reversible reaction is performed as follows:

$$Ca_{10}(PO_4)_6OH_2 \rightarrow Ca_{10}(PO_4)_6OH_{2-2x}O_x + xH_2O_{gas}.$$
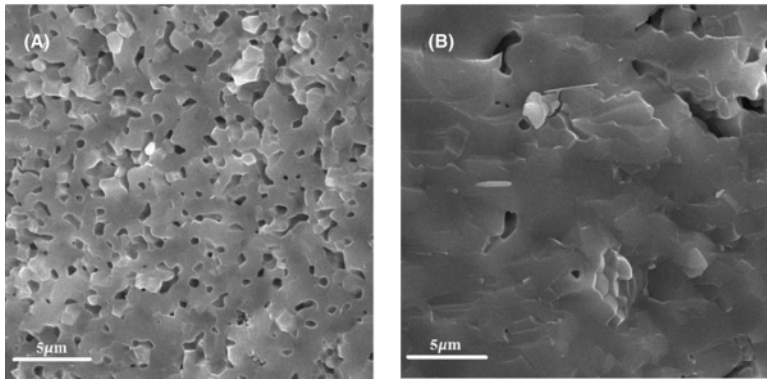
4 SEM images of (A) HA scaffold (cross-sectional view) and (B) HA/MnO₂ scaffold (cross-sectional view)

HA was decomposed to TCP or TTCP with the following reaction at temperatures above 900°C:

$$Ca_{10}(PO_4)_6OH_2 \rightarrow 2Ca_3(PO_4)_2 + Ca_4P_2O_9 + H_2O_{gas}.$$
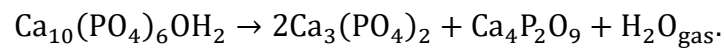
In Figure 4A, porosity formation can be due to dehydroxylation within the HA matrix. Dehydroxylation is achieved by releasing OH ions in a wide range of temperatures, and it is reported to depend on partial pressure of H2O during heating. Thus, for HA, slight dehydroxylation can occur. With further increase in temperature, HA dehydration may continue, resulting in the formation of internal vapor pressure in closed vents near the free surface of the HA sample. In Figure 4B, when the MnO₂ powder is precipitated on the HA, the particle fusion is increased. In this way, there is very low porosity in the HA/MnO₂ sample. In short, MnO₂ helps sintering of two-phase calcium phosphate. This can be applied to the use of two-phase calcium phosphate powders for bone implantation, because denser implants have better mechanical strength.[19,39]

TEM images

The morphology of pure HA and HA/MnO₂ powders was investigated by TEM (Figure 5A,B). It is observed that particles have a spherical shape. HA spherical particles have dimensions less than 100 nm (Figure 5A). Figure 5B also shows the white precipitates on these particles that are less than 10 nm and are indicated by an arrow on the Figure 5B.
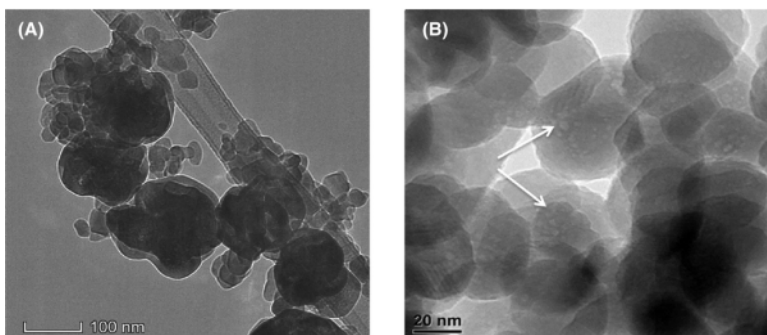

5 TEM image of HA/MnO₂ powder

TG/DTA analysis

Figure 6 shows the weight loss of total water present in the crystalline HA network, a reduction in the weight associated with the HA mineral composition analysis is also shown. The full graph (TGA)

represents three almost linear regions: the temperature ranges of 100-400°C and 600-800°C, with a low dehydroxylation rate and a temperature range of 800-900°C, with high dehydroxylation rates. The kinetics indicate that dehydroxylation generally occurs at high temperatures, but 800°C is a reasonable amount for assigning a small amount of dehydroxylation rate.[40] This is in agreement with the research by Santos et al.[41] The TGA chart consists of three steps: from ambient temperature up to 200°C, 400-600°C, and 800-900°C. The first step is the evaporation of moisture, the oxidation of sediment solvents, and pre-mineral decomposition at a temperature of 200°C. Extensive endothermic peak was observed in the DSC curve (Figure 6) at about 50°C, which was attributed to water loss. The dashed line graph (DSC) has an exothermic peak in this temperature range, which indicates the evaporation process. In the first step, the HA/MnO$_2$ mass is slowly decreased by 0.2%, which is related to the removal of water absorbed on the composite surface and the loss of water in the network.[26] In the second step, a weight loss of up to 1% is observed, which is related to the decomposition of the mineral compounds associated with HA. In the third step, a significant drop in weight of 0.5% was observed at temperature above 800°C, indicating that the synthesized HA was heated to higher temperatures at 800°C and then decomposed into secondary phases such as TCP, and the processed product will be two-phase calcium Phosphate. The dashed line graph has an exothermic peak (DSC analysis in Figure 6) in this temperature range, which illustrates this process.
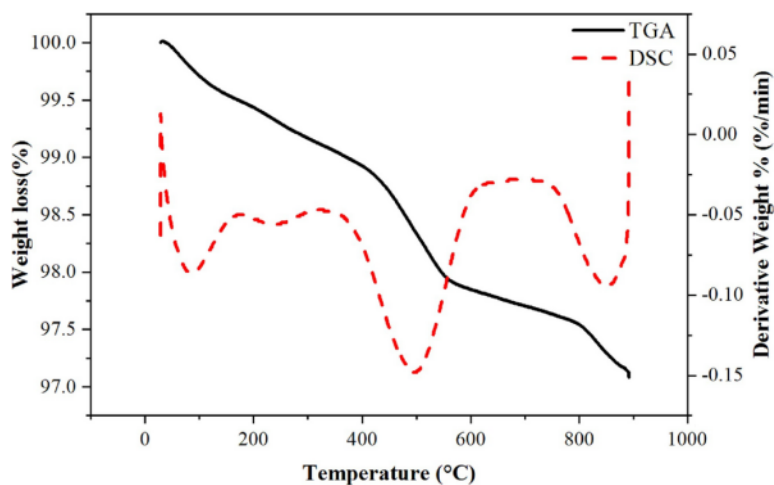
6 TG/DSC analysis of HA/MnO$_2$ composite powder

Mechanical testing

Heidari et al reported that HA samples extracted from the cattle bone—pressed with a CIP method and sintered at 1300°C—have a compressive strength of 3.25 MPa and a toughness of 0.3 MPa.[27] However, in this study, with the same manufacturing conditions, the compressive strength of the pure HA sample obtained is 13.02 MPa, while the toughness is reduced to 0.14 MPa (Table 1). Furthermore, hardness in these specimens has been shown to increase by 0.6 GPa than those made from natural HA. These changes are likely due to the HA powder, which had been synthesized by the sol-gel method, and the size of the powder was smaller compared to HA used in our previous study.[27] Addition of MnO$_2$ to HA results in an increase in hardness (from 3.9 to 4.8 GPa), an increase in density (from 2.83 to 2.97 g/cm^3) which SEM images also confirm (Figure 4), an increase in compressive strength (from 13.02 to 13.87 MPa), and an increase the toughness (from 0.14 to 0.28 MPa) of the samples ($P < .05$). Hence, our results show that MnO$_2$ increases the fracture energy of the samples due to the condensation of

the samples under the same conditions of production. The percentage of increase in compressive strength of pure HA to MnO_2/HA was 6.5%. This increase in compressive strength was also predictable with SEM images (Figure 4) as the porosity of pure HA scaffold decreased with the addition of MnO_2. Bone compressive strength is 2-10 MPa.[42,43] Therefore, in this study, both pure HA and MnO_2/HA scaffolds have higher compressive strength than bone, so the toughness of each one is important. The MnO_2/HA toughness is twice that of pure HA, which means that the energy absorption up to the fracture of the MnO_2/HA scaffolds is greater than that of pure HA. Also, the origin of the blue HA after the precipitation of MnO_2 and sintering at 1300°C is due to the presence of Mn^{5+} or MnO_4^{3-} ions in PO_4^{3-} sites in the crystalline apatite structure. According to authors, high temperatures not only increase the oxidation intensity in the oxidizing atmosphere, but also provide enough energy for oxidized Mn ions to facilitate their migration to the crystal network. This color change caused by ions migration has a good effect on increasing the mechanical properties of the HA/MnO_2 composite.[39] Ramesh et al[39] showed that the addition of 0.05% Manganese oxide to HA with a sintering temperature of 1100-1000°C leads to an increase in the hardness of HA, especially for samples that are sintered at temperatures below 1000°C. It was therefore predictable that the surface modification of the HA powder with MnO_2 would increase its hardness.

1 TABLE. Mechanical properties of HA and MnO_2 -modified HA scaffolds

|	Compressive strength (MPa)	Toughness (MPa)	Hardness (GPa)	Density (g/cm^3)
HA	13.02 ± 0.15	0.14 ± 0.03	3.9 ± 0.1	2.83
HA/MnO_2	13.87 ± 0.17	0.28 ± 0.05	4.8 ± 0.1	2.97

Figure 7A,B show compressive stress-strain diagrams for scaffolds. It can be seen that in each chart, the stress has been steadily increasing, and this ascending trend continues so that samples cannot withstand the stress, and crack. After cracking the samples, there is a sharp drop in the stress. Maximum compressive strength is considered at the point where stress begins to decrease. Figure 7 shows that with the deposition of MnO_2 on HA, the compressive strength of composite samples is increased in comparison to pure HA, which is due to the high strength of MnO_2 compared to the HA in the composite.[44]
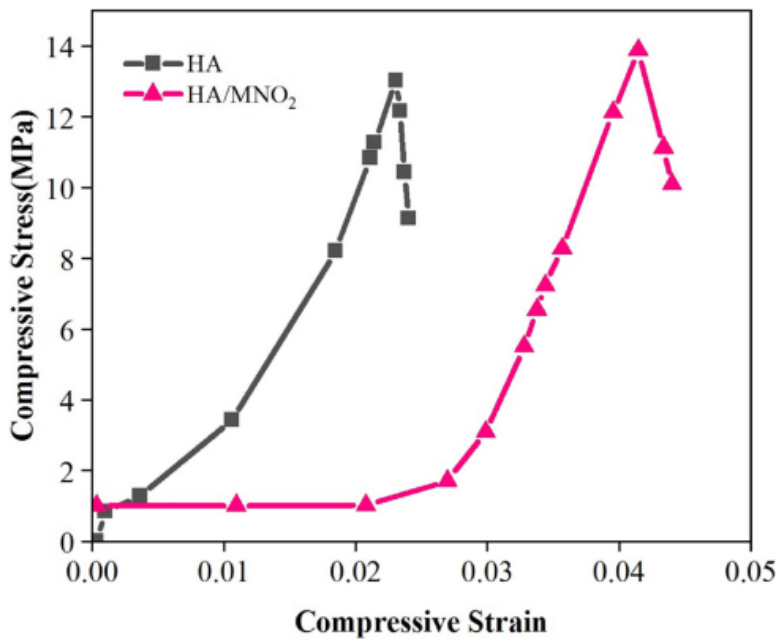
7 Compressive stress-strain curve of pure HA and HA/MnO₂ scaffolds

Immersion in SBF solution

Figure 8a-c indicates the SEM images of HA and HA/MnO₂ after 28 days immersion in SBF. Figure 8A,B show that apatite deposition on pure HA is completely uniform, but Figure 8C indicates the increase in the surface roughness of HA/MnO₂.
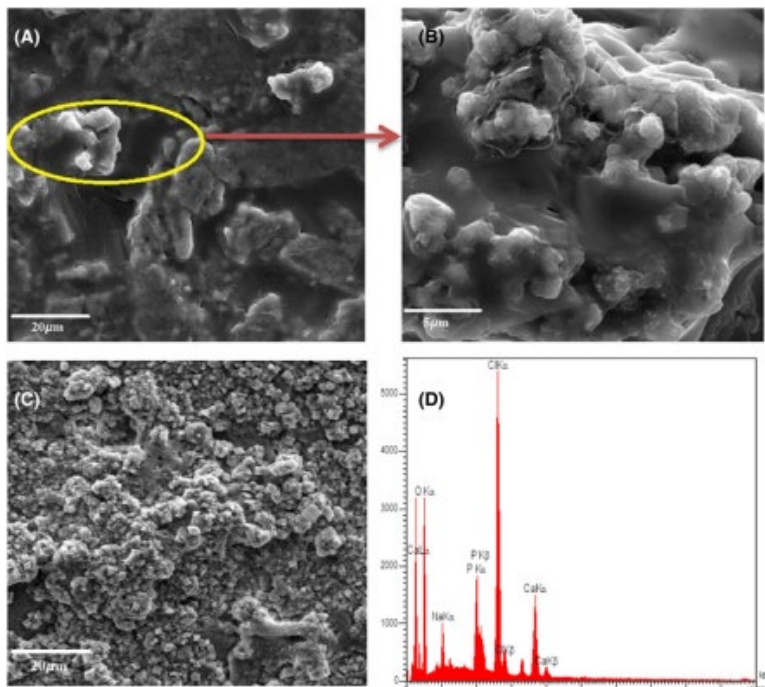
8 SEM images from the surface of the scaffold after 28 days of immersion in SBF solution, (A) pure HA, (B) HA with higher magnification, (C) HA/MnO₂, (D) EDAX analysis of the deposited layer on the surface of HA/MnO₂ scaffold

The formed apatite has been further analyzed and confirmed by EDAX, showing the main elements are calcium and phosphorus (Figure 8D). Also, other elements (chlorine and sodium) are detected in our EDAX analysis, which can be due to the NaCl in the SBF solution.

The surface roughness of the HA scaffolds is shown in Figure 9A. The mean roughness of the samples before and after immersion in SBF indicated in Table 2. Figure 9B shows the AFM graph of HA/MnO$_2$, when the roughness of MnO$_2$ deposited on HA has decreased from 955.2 to 423.5 nm (Table 2). Figure 9C shows the AFM graph of the surface of the pure HA sample after immersion. Surface roughness decreases by 338.4 nm, compared to before immersion. Figure 9D shows the surface of the HA/MnO$_2$ sample. The surface roughness in this sample has increased from 423.5 to 460.4 nm (Table 2). Our results show that MnO$_2$ can increase apatite deposition on the surface of HA scaffolds. Usually at roughness more than 50 nm, van der Waals forces are the main factor; while at closer distances (10-20 nm), a combination of both van der Waals forces and electrostatic interactions controls cell adhesion.[45] For metals used in medical implants, the desired surface roughness is usually below 10 nm.[46] Rough surface promotes friction, thus reduces the mobility of the bacteria; this sessile environment facilitates the biofilm growth.[47] Hence, HA and HA/MnO$_2$ have a significant surface roughness and can be a good place for cell proliferation.
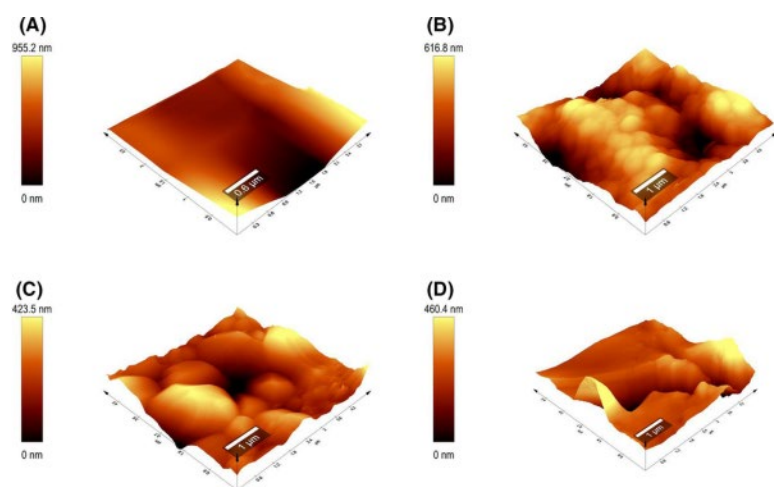
9 Analysis of surface topography using AFM from (A) surface of pure HA scaffold before immersion, (B) surface of HA/MnO$_2$ scaffold before immersion, (C) surface of pure HA scaffold after immersion and (D) surface of HA/MnO$_2$ scaffold after immersion in the SBF solution

2 TABLE. Amount of roughness of surface samples

| Samples	Surface roughness before immersion (nm)	Surface roughness after immersion (nm)	Change in roughness (nm)
HA	995.2	616.8	−338.4
HA/MnO$_2$	423.5	460.4	+36.9

Cell culture

ALP is believed to be upregulated in the early stages of biomineralization in order to form a large pool of inorganic phosphate from which HA can be mineralized.[48] After the onset of mineralization, ALP is no longer needed, and therefore, cellular levels of the enzyme drop before a mature mineralized

matrix is formed.[49] Figure 10 shows the results of ALP after 14 days. The average data show the activity of ALP for pure HA is more than HA/MnO$_2$ scaffolds.
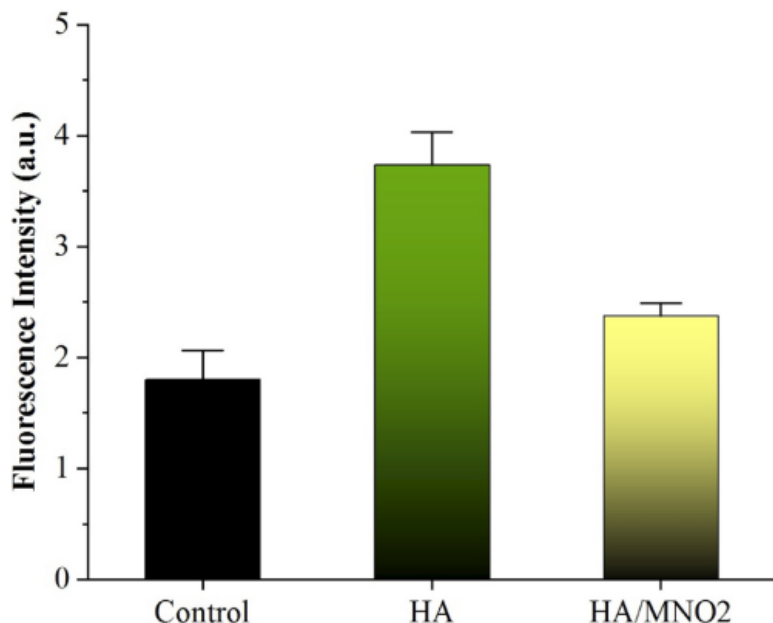

10 ALP assessment on HA and HA/MnO$_2$ scaffolds (14 days)

Figure 11 shows the proliferation of human osteoblast cells on the surface of the scaffold. Darker graphs appear after 7 days, and clearer graphs after 14 days in the culture medium. Both samples show more cell proliferation after 14 days than 7 days. Generally, the proliferation of cells on pure HA is higher than that of HA/MnO$_2$, but both samples show good viability after 7 days compared to the control sample. In such conditions, we should know that at some concentrations, Mn ions could also have negative effects on the cells.[50] Lower cell proliferation of MnO$_2$/HA is probably due to the faster and higher ion release such as Mn from the porous scaffolds compared with the pure HA.51 Future studies are recommended for measurement of the released Mn ion from HA/MnO$_2$ constructs and screening the best concentration. Furthermore, the efficacy of these samples against different bacteria might be assessed.
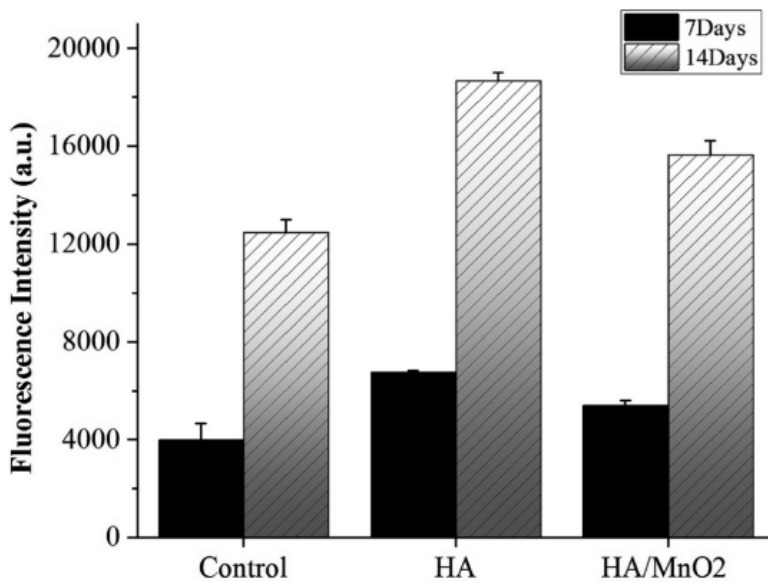
11 Cell proliferation diagrams on HA and HA/MnO$_2$ scaffolds after 7 and 14 days

Figure 12 shows SEM images of human osteoblast cells attached to the surface of the specimens after 14 days, confirming the biocompatibility of our HA and HA/MnO$_2$ scaffolds. According to SEM observations, the human osteoblast cells retaining spindle morphology on the scaffolds. The osteoblast cells projections and pseudopodia were detected and, fibrous extracellular matrix (ECM) was observed. The SEM images indicated that the scaffolds maintained cellular adhesion, spread, and proliferation. Such observation implies that the scaffolds well supported normal cell metabolism with favorable biocompatibility in vitro.
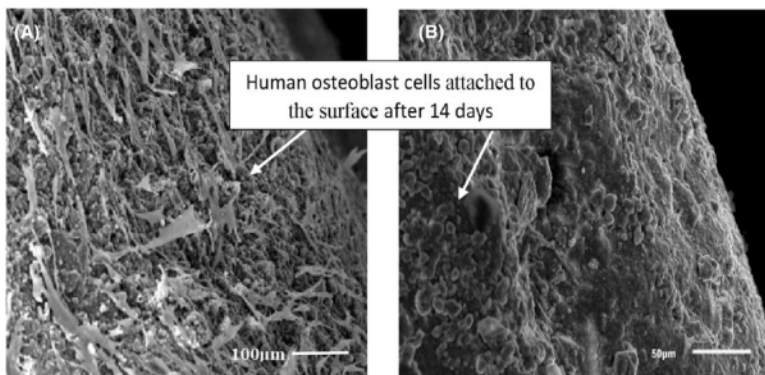
12 SEM images from the cells attached to the surface of the specimens after 14 days of culture: (A) HA/MnO$_2$ scaffold, (B) pure HA scaffold

CONCLUSION

HA powder was synthesized by sol-gel method and modified with MnO$_2$ deposition. Scaffolds were then made using CIP method, followed by sintering at 1300°C. With the addition of MnO$_2$ to HA, the compressive strength increased by 6.5% and the toughness doubled. The samples also became denser and the density increased by 4.95%. After immersion in the SBF solution, results of SEM images show that the HA/MnO$_2$ scaffold is rougher than the pure HA one. The results of cell attachment and proliferation prove the biocompatibility of our HA/MnO$_2$ bioscaffolds.

ACKNOWLEDGMENT

REFERENCES

1. Jabbarpour BM, Mahdavi N. Studying the effect of mitogen activated protein kinase inhibitor (mapki) on mesenchymal stem cells in vitro. Pharmaceutical Sciences. 2005; 3: 39 – 44.
2. Johnson A, Moutray M, Hoffmann W. Effect of ethylene oxide sterilization and storage conditions on canine cortical bone harvested for banking. Vet Surg. 1987; 16 (6): 418 – 22.
3. Johnson A, Shokry M, Stein L. Preliminary study of ethylene oxide sterilization of full-thickness cortical allografts used in segmental femoral fracture repair. Am J Vet Res. 1985; 46 (5): 1050 – 6.
4. Hench L, Wilson J. Introduction to Bioceramics. World Sci: Publ Co. New Jersey: EUA; 1993.
5. Rho J-Y, Kuhn-Spearing L, Zioupos P. Mechanical properties and the hierarchical structure of bone. Med Eng Phys. 1998; 20 (2): 92 – 102.
6. Boccaccini AR, Ma PX. Tissue Engineering using Ceramics and Polymers. Second, UK: Elsevier; 2014.
7. Heidari F, Razavi M, Bahrololoom ME, Bazargan-Lari R, Vashaee D, Kotturi H, et al. Mechanical properties of natural chitosan/hydroxyapatite/magnetite nanocomposites for tissue engineering applications. Mater Sci Eng, C. 2016; 65: 338 – 44.
8. Woodard JR, Hilldore AJ, Lan SK, Park C, Morgan AW, Eurell JAC, et al. The mechanical properties and osteoconductivity of hydroxyapatite bone scaffolds with multi-scale porosity. Biomaterials. 2007; 28 (1): 45 – 54.
9. Azami M, Rabiee M, Moztarzadeh F. Glutaraldehyde crosslinked gelatin/hydroxyapatite nanocomposite scaffold, engineered via compound techniques. Polym Compos. 2010; 31 (12): 2112 – 20.
10. Heymann D, Passuti N. Bone substitutes: new concepts. Eur J Orthop Surg Traumatol. 1999; 9 (3): 179 – 84.
11. Silva V, Lameiras F. Synthesis and characterization of composite powders of partially stabilized zirconia and hydroxyapatite. Mater Charact. 2000; 45 (1): 51 – 9.
12. Hu Z, Zhao Y, Liu J, Wang J, Zhang B, Xiang X. Ultrafine MnO 2 nanoparticles decorated on graphene oxide as a highly efficient and recyclable catalyst for aerobic oxidation of benzyl alcohol. J Colloid Interface Sci. 2016; 483: 26 – 33.
13. Ahmad K, Mohammad A, Mobin SM. Hydrothermally grown α-MnO 2 nanorods as highly efficient low cost counter-electrode material for dye-sensitized solar cells and electrochemical sensing applications. Electrochim Acta. 2017; 252: 549 – 57.
14. Deka K, Guleria A, Kumar D, Biswas J, Lodha S, Kaushik SD, et al. Mesoporous 3D carbon framework encapsulated manganese oxide nanoparticles as biocompatible T1 MR imaging probe. Colloids Surf, A. 2018; 539: 229 – 36.
15. Guo W, Qi Y, Zhang Y, Ma L, Yu D, Zhan J. Biocompatible caramelized carbonaceous nanospheres supported paramagnetic ultrathin manganese oxide nanosheets via self-sacrificing reduction as a MRI contrast agent for liver imaging. Carbon. 2016; 110: 321 – 9.
16. Sarkar A, Satpati AK, Kumar V, Kumar S. Sol-gel synthesis of manganese oxide films and their predominant electrochemical properties. Electrochim Acta. 2015; 167: 126 – 31.

17. Dong L, Zhu Z, Qiu Y, Zhao J. Removal of lead from aqueous solution by hydroxyapatite/manganese dioxide composite. Frontiers Environmental Science Engineering. 2016; 10 (1): 28 – 36.
18. Mayer I, Diab H, Reinen D, Albrecht C. Manganese in apatites, chemical, ligand-field and electron paramagnetic resonance spectroscopy studies. J Mater Sci. 1993; 28 (9): 2428 – 32.
19. Natasha A, Sopyan I, Zuraida A. Fourier transform infrared study on sol-gel derived manganese-doped hydroxyapatite. Adv Materials Res; 2008; 47-50: 1185 – 8.
20. Takeda A. Manganese action in brain function. Brain Res Rev. 2003; 41 (1): 79 – 87.
21. Saxena V, Shukla I, Pandey LM. Hydroxyapatite: an inorganic ceramic for biomedical applications, Chapter 8. In: Materials for biomedical engineering. Amsterdam: Elsevier, 2019; p. 205 – 249. https://0-doi-org.libus.csd.mu.edu/10.1016/B978-0-12-816909-4.00008-7
22. Mayer I, Cuisinier FJG, Popov I, Schleich Y, Gdalya S, Burghaus O, et al. Phase relations between β-tricalcium phosphate and hydroxyapatite with manganese (ii): structural and spectroscopic properties. Eur J Inorg Chem. 2006; 2006 (7): 1460 – 5.
23. Foroughi MR, Karbasi S, Sajadi MA. Novel sol–gel synthesis and characterization of nanostructured hydroxyapatite powder. J Mater Sci. 2010; 1: 36 – 44.
24. Otitoju TA, Okoye PU, Chen G, Li Y, Okoye MO, Li S, et al. Advanced ceramic components: materials, fabrication, and applications. J Ind Eng Chem. 2020.
25. Tadic D, Epple M. Mechanically stable implants of synthetic bone mineral by cold isostatic pressing. Biomaterials. 2003; 24 (25): 4565 – 71.
26. Monmaturapoj N, Luang K. Nano-size hydroxyapatite powders preparation by wet-chemical precipitation route. Metals, Materials Minerals. 2008; 18 (1): 15 – 20.
27. Shaabani A, Afaridoun H, Shaabani S. Natural hydroxyapatite-supported MnO 2: a green heterogeneous catalyst for selective aerobic oxidation of alkylarenes and alcohols. Appl Organomet Chem. 2016; 30 (9): 772 – 6.
28. Heidari F, Razavi M, Ghaedi M, Forooghi M, Tahriri M, Tayebi L. Investigation of mechanical properties of natural hydroxyapatite samples prepared by cold isostatic pressing method. J Alloys Compounds. 2017; 693: 1150 – 6.
29. Kumar A, Biswas K, Basu B. On the toughness enhancement in hydroxyapatite-based composites. Acta Mater. 2013; 61 (14): 5198 – 215.
30. Kim YG, Seo DS, Lee JK. Dissolution of synthetic and bovine bone-derived hydroxyapatites fabricated by hot-pressing. Appl Surf Sci. 2008; 255 (2): 589 – 92.
31. Heidari F, Bahrololoom ME, Vashaee D, Tayebi L. In situ preparation of iron oxide nanoparticles in natural hydroxyapatite/chitosan matrix for bone tissue engineering application. Ceramics International. 2015; 41 (2, Part B): 3094 – 100.
32. Heidari F, Razavi M, E.Bahrololoom M, Bazargan-Lari R, Vashaee D, Kotturi H, et al. Mechanical properties of natural chitosan/hydroxyapatite/magnetite nanocomposites for tissue engineering applications. Mater Sci Eng, C. 2016; 65: 338 – 44.
33. Lee DS, Pai Y, Chang S. Effect of thermal treatment of the hydroxyapatite powders on the micropore and microstructure of porous biphasic calcium phosphate composite granules. J Biomaterials Nanobiotech. 2013; 4 (02): 114.
34. Saadat A, Karbasi S, Behnamghader A, Radmehr M, Sadeghi M, Forooghi M. Preparation and structural assessement of PHB/nHA composite scaffold used in bone tissue engineering. Adv Processes Materials. 2012; 6 (1): 11 – 23.

35. Sagadevan S, Dakshnamoorthy A. Synthesis and characterization of nano-hydroxyapatite (n-HAP) using the wet chemical technique. International Journal of Physical Sciences. 2013; 8 (32): 1639 – 45.

36. Chahkandi B, Chahkandi M. The effects of sol-gel process parameters on the phase purity of hydroxyapatite. J Applied Chem Res. 2010; 13.

37. Yoruç ABH, Aydınoğlu A. The precursors effects on biomimetic hydroxyapatite ceramic powders. Mater Sci Eng, C. 2017; 75: 934 – 46.

38. Royer A, Viguie J, Heughebaert M, Heughebaert J. Stoichiometry of hydroxyapatite: influence on the flexural strength. J Mater Sci - Mater Med. 1993; 4 (1): 76 – 82.

39. Wang PE, Chaki T. Sintering behaviour and mechanical properties of hydroxyapatite and dicalcium phosphate. J Mater Sci - Mater Med. 1993; 4 (2): 150 – 8.

40. Ramesh S, Tan C, Peralta C, Teng W. The effect of manganese oxide on the sinterability of hydroxyapatite. Science Technology Adv Materials. 2007; 8 (4): 257 – 63.

41. Ruys A, Wei M, Sorrell C, Dickson M, Brandwood A, Milthorpe B. Sintering effects on the strength of hydroxyapatite. Biomaterials. 1995; 16 (5): 409 – 15.

42. Santos J, Morrey S, Hastings G, Monteiro F. editors. The production and characterisation of a hydroxyapatite ceramic material. Bioceramics: Proceedings of the 4th International Symposium on Ceramics in Medicine London, UK, September 1991: Elsevier.

43. Pu X-M, Wei K, Zhang Q-Q. In situ forming chitosan/hydroxyapatite rods reinforced via genipin crosslinking. Mater Lett. 2013; 94: 169 – 71.

44. Hutmacher DW. Scaffolds in tissue engineering bone and cartilage. Biomaterials. 2000; 21 (24): 2529 – 43.

45. Ragurajan D, Golieskardi M, Satgunam M, Hoque ME, Ng AMH, Ghazali MJ, et al. Advanced 3Y-TZP bioceramic doped with Al 2 O 3 and MnO 2 particles potentially for biomedical applications: study on mechanical and degradation properties. J Materials Res Technology. 2018; 7 (4): 432 – 42.

46. Percival SL, Malic S, Cruz H, Williams DW. Introduction to biofilms. In: Percival S, Knottenbelt D, Cochrane C, editors. Biofilms and Veterinary Medicine. Berlin Heidelberg: Springer; 2011. p. 41 – 68.

47. Mendonca G, Mendonca DB, Aragao FJ, Cooper LF. Advancing dental implant surface technology – from micron- to nanotopography. Biomaterials. 2008; 29 (28): 3822 – 35.

48. Golabi M, Turner APF, Jager EWH. Tunable conjugated polymers for bacterial differentiation. Sensors and Actuators B: Chemical. 2016; 222: 839 – 48.

49. Anderson HC. Molecular biology of matrix vesicles. Clin Orthop Relat Res. 1995; 314: 266 – 80.

50. Boyan BD, Schwartz Z, Swain LD. Cell maturation-specific autocrine/paracrine regulation of matrix vesicles. Bone and Mineral. 1992; 17 (2): 263 – 8.

51. Ma Z, Gao M, Na D, Li Y, Tan L, Yang K. Study on a biodegradable antibacterial Fe-Mn-C-Cu alloy as urinary implant material. Mater Sci Eng, C. 2019; 103: 109718.

52. Feng YP, Gaztelumendi N, Fornell J, Zhang HY, Solsona P, Baró MD, et al. Mechanical properties, corrosion performance and cell viability studies on newly developed porous Fe-Mn-Si-Pd alloys. J Alloy Compd. 2017; 724: 1046 – 56.